CRYSTAL GROWTH & DESIGN

Article

Cite This: *Cryst. Growth Des.* 2020, 20, 1079−1087

pubs.acs.org/crystal

Crystal Structures, Stability, and Solubility Evaluation of Two Polymorphs of a 2:1 Melatonin−Piperazine Cocrystal

Yan Yan,[‡] Xia-Lin Dai,[§] Jun-Long Jia,[†] Xing-Hua Zhao,[∥] Zhi-Wei Li,[⊥] Tong-Bu Lu,[†] and Jia-Mei Chen*[,†]

[†]School of Chemistry and Chemical Engineering, Institute for New Energy Materials and Low Carbon Technologies, Tianjin University of Technology, Tianjin 300384, China

[‡]School of Chemistry & Materials Science, Jiangsu Key Laboratory of Green Synthetic Chemistry for Functional Materials, Jiangsu Normal University, Xuzhou 221116, China

[§]School of Pharmaceutical Sciences, Sun Yat-Sen University, Guangzhou 510006, China

[∥]College of Veterinary Medicine, Hebei Agricultural University, Baoding 071000, China

[⊥]National Supercomputing Center in Shenzhen (Shenzhen Cloud Computing Center), Shenzhen 518000, China

Supporting Information

ABSTRACT: The polymorphism of cocrystals is not studied as widely as that of single-component crystals. In this work, two polymorphic forms of a cocrystal of melatonin with piperazine (**MLT−PIP I** and **MLT−PIP II**) in a 2:1 stoichiometry were successfully obtained and fully characterized. The crystal structures exhibit differences in hydrogen bonding modes and molecular packing arrangements across two polymorphs. Theoretical computations were carried out to compare their crystal lattice energy. They were also evaluated by thermal analysis, variable temperature X-ray powder diffraction, and dynamic vapor sorption measurements, as well as powder and intrinsic dissolution experiments. The results of experimental and theoretical studies conclude that **MLT−PIP II**, as the stable form, exhibits a significantly improved solubility and dissolution rate and is suitable to be developed into a more efficient formulation of melatonin.

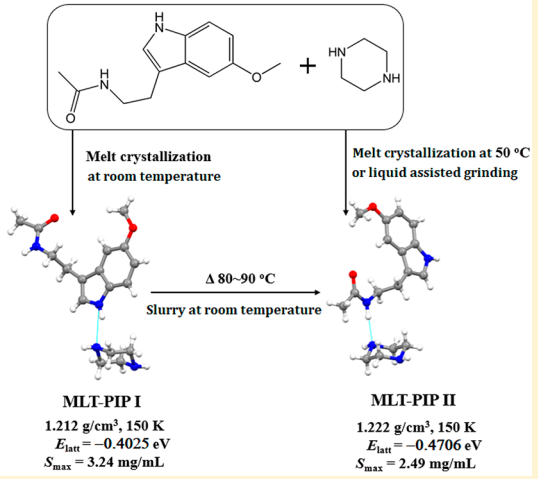

INTRODUCTION

Polymorphism refers to the ability that a compound can exist in multiple crystalline phases with different molecular conformations and/or crystal packing arrangements in the crystal lattices, which is a universal and important phenomenon for solid pharmaceutical.[1] Pharmaceutical polymorphs exhibit different physicochemical properties, including melting point, solubility, dissolution rate, stability, processability, etc., among each other.[2−7] Therefore, polymorphism offers an opportunity to investigate the relationship of structure and property for a given drug with different crystal structures. Pharmaceutical cocrystals are crystalline single phase solids composed of a drug and one or more cocrystal formers in a stoichiometric ratio, which are usually used in pharmaceutical industry to improve physical and chemical properties of drugs without changing their molecular structures. Polymorphs of single-component pharmaceutical compounds have been reported widely.[8−13] However, the occurrence of polymorphism for pharmaceutical cocrystals has not been so extensively studied.[14−19] Only limited work has focused on studying polymorphs of pharmaceutical cocrystals, although they are universally used for drug development and manufacture.[14−19] Thus, it is of great importance to identify and evaluate polymorphic forms of pharmaceutical cocrystals in the pharmaceutical field.

Melatonin (MLT, Scheme 1) is a natural hormone produced by the pineal gland in mammals.[20] It exhibits various physiological functions, such as circadian rhythm and sleep regulation,[21] immunostimulative activity,[22] mood modulation,[23] and

Scheme 1. Chemical Structures of Melatonin (MLT) and Piperazine (PIP)

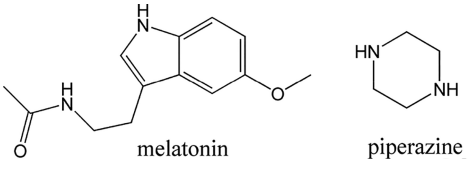

Received: October 20, 2019
Revised: November 26, 2019
Published: December 24, 2019

DOI: 10.1021/acs.cgd.9b01405
Cryst. Growth Des. 2020, 20, 1079−1087

cytoprotective activity.[24] MLT is also a wide-spectrum antioxidant and has potential therapeutic effects in treating neurodegenerative diseases and a variety of cancers.[25] Exogenous MLT is orally applied as a dietary supplement for delayed sleep phase syndrome, shift work disorder, and jet lag.[26] MLT is a BCS class II drug with poor solubility and good permeability.[27] The application of MLT as a drug in the clinic is severely restricted by its poor and variable oral absorption due to its low solubility.[28] Therefore, improving the solubility of MLT is highly desirable for drug development. We have reported a cocrystal of MLT with pimelic acid exhibiting a 2-fold increase in solubility.[29] Two cocrystals of piperazine and 1,4-diazabicyclo[2.2.2] octane as well as an ionic cocrystal with $CaCl_2$ have also been reported recently.[30] However, only the solubility of the ionic cocrystal has been tested, and it showed a 10-fold increase with respect to the pure drug. The single crystal structure and physicochemical property of the cocrystal with piperazine were not studied in detail.[30]

From the perspective of a supramolecular structure, the MLT molecule has one amide group and one indole group, and can act both as the acceptor and the donor of hydrogen bonds. It may form polymorphic forms when cocrystallizing with other compounds, due to different intermolecular hydrogen bonding patterns and molecular packing possibly generated. In this work, two polymorphs of the cocrystal of MLT with piperazine (PIP, Scheme 1) in a 2:1 stoichiometric ratio were successfully synthesized via the melt crystallization method.[31] The single crystal structures of the two polymorphs were determined and resolved. The density functional theory computations based on the single crystal structures were performed to compare the crystal lattice energies of these two forms. They were also investigated by variable temperature X-ray powder diffraction, thermal analysis and dynamic vapor sorption measurements, as well as powder and intrinsic dissolution experiments.

EXPERIMENTAL SECTION

Preparation of MLT−PIP Cocrystal (2:1) Form I, MLT−PIP I. MLT (50 mg, 0.2 mmol) was completely melted at 135 °C, and then PIP (9.1 mg, 0.1 mmol) was added. After complete melting of all the solids, the molten was cooled under room temperature. The white crystalline powder was produced from the crystallization of the molten sample. Single crystals of **MLT−PIP I** were obtained by slow evaporation of **MLT−PIP I** from ethyl acetate solution with crystal seeds. Anal. (%) Calcd for $C_{15}H_{21}N_3O_2$: C, 65.43; H, 7.68; N, 15.26%. Found: C, 65.12; H, 7.71; N, 15.16%. IR (KBr, ν): 3317 (s), 3209 (s), 3278 (s), 2949 (s), 2222 (w), 1874 (w), 1639 (s), 1583 (s), 1487 (s), 1444 (s), 1361 (m), 1300 (s), 1271 (m), 1232 (s), 1220 (s), 1201 (s), 1176 (m), 1126 (m), 1099 (m), 1072 (s), 1034 (s), 1001 (m), 962 (w), 924 (m), 852 (s), 808 (s), 766 (m), 714 (w), 679 (m), 644 (m), 588 (m), 526 (w), 503 (w), 463 (m), 442 (m) cm^{-1}.

Preparation of MLT−PIP Cocrystal (2:1) Form II, MLT−PIP II. **MLT−PIP II** was prepared by two methods: (i) MLT (50 mg, 0.2 mmol) was completely melted at 135 °C, and then PIP (9.1 mg, 0.1 mmol) was added. After complete melting of all the solids, the molten was allowed to cool under 50 °C. The white crystalline powder was derived from the crystallization of molten sample. (ii) The experiment of liquid-assisted grinding was carried out by adding a mixture of MLT (50 mg, 0.2 mmol) and PIP (9.1 mg, 0.1 mmol) with one drop of methanol into a 25 mL stainless steel grinding jar. The mixture was then ground using a Retsch MM 200 mixer mill for 30 min at a frequency of 20 Hz. The crystalline powder of **MLT−PIP II** from melt crystallization was completely dissolved in ethyl acetate, and then the solution was slowly evaporated to obtain single crystals. Anal. (%) calcd for $C_{15}H_{21}N_3O_2$: C, 65.43; H, 7.68; N, 15.26%. Found: C, 65.34; H, 7.67; N, 15.05%. IR (KBr, ν): 3315 (s), 3246 (s), 3035 (m), 3003 (m), 2949 (s), 2831 (s), 2750 (m), 2144 (w), 2054 (w), 1874 (w), 1641 (s), 1583 (s), 1485 (s), 1444 (s), 1360 (m), 1300 (s), 1219 (s), 1174 (m), 1126 (m), 1099 (m), 1072 (s), 1034 (s), 985 (w), 962 (w), 924 (s), 850 (s), 806 (s), 766 (m), 679 (m), 642 (m), 588 (m), 525 (w), 461 (m), 440 (w) cm^{-1}.

Table 1. Crystallographic Data and Refinement Parameters for MLT−PIP I and MLT−PIP II

	MLT−PIP I	MLT−PIP II
formula	$C_{15}H_{21}N_3O_2$	$C_{15}H_{21}N_3O_2$
formula weight	275.35	275.35
temperature (K)	150(2)	150(2)
crystal size (mm^3)	0.30 × 0.20 × 0.20	0.20 × 0.10 × 0.10
crystal system	monoclinic	monoclinic
space group	$P2_1/c$	$P2_1/n$
a (Å)	17.0514(8)	8.7944(3)
b (Å)	9.8333(4)	13.0770(4)
c (Å)	9.3217(4)	13.2694(4)
α (deg)	90	90
β (deg)	105.084(4)	101.324(3)
γ (deg)	90	90
volume ($Å^3$)	1509.13(11)	1496.33(8)
Z	4	4
density ($g·cm^{-3}$)	1.212	1.222
$F(000)$	592	592
index ranges	$-19 \le h \le 18$	$-10 \le h \le 9$
	$-10 \le k \le 11$	$-12 \le k \le 14$
	$-7 \le l \le 10$	$-12 \le l \le 15$
no. of reflns	5118	5163
no. of unique reflns	2409	2370
no. of params	210	195
R_{all}, R_{obs} [a]	0.0579, 0.0447	0.0665, 0.0471
$wR_{2,all}$, $wR_{2,obs}$ [a]	0.1372, 0.1263	0.1272, 0.1127
GOF	1.038	1.035

[a] $R_1 = \Sigma||F_o| - |F_c||/\Sigma|F_o|$.

$wR_2 = [\Sigma[w(F_o^2 - F_c^2)^2]/\Sigma w(F_o^2)^2]^{1/2}$,

$w = 1/[s^2(F_o)^2 + (aP)^2 + bP]$,

where $P = [(F_o^2) + 2F_c^2]/3$.

Table 2. Hydrogen Bonding Distances and Angles for MLT−PIP I and MLT−PIP II

	hydrogen bond	H···A (Å)	D···A (Å)	∠D−H···A (deg)
MLT−PIP I [a]	N2−H2···N3	0.86	2.976(4)	157.2
	N1−H1···O1#1	0.86	2.970(2)	166.2
MLT−PIP II [b]	N1−H1···N3	0.97(3)	2.911(3)	171(3)
	N2−H2···O1#2	0.87(3)	2.842(3)	158(2)

[a] Symmetry codes. #1 $-x + 1, y + 1/2, -z + 1/2$. [b] #2 $x - 1/2, -y + 3/2, z - 1/2$.

Solubility and Intrinsic Dissolution Rate (IDR). The absorbance values for MLT were detected by a Cary 50 UV−vis spectrophotometer at 230 nm, where PIP does not interfere with the determination. For solubility and IDR measurements involving MLT, **MLT−PIP I** and **MLT−PIP II**, absorbance values were related to MLT concentrations using a calibration curve.

All the solids were milled to powder and sieved with standard mesh sieves to control the particle size range of approximately 75−150 μm. In a typical powder dissolution experiment, 300 mg of sample was added into 50 mL of phosphate buffer (pH 6.8) in the flask, and the resulting suspension was stirred at 500 rpm and 37 °C. At predetermined time intervals, an aliquot of the slurry was withdrawn and filtered by a 0.22 μm nylon filter. A 10 μL portion of the filtered

DOI: 10.1021/acs.cgd.9b01405
Cryst. Growth Des. 2020, 20, 1079−1087

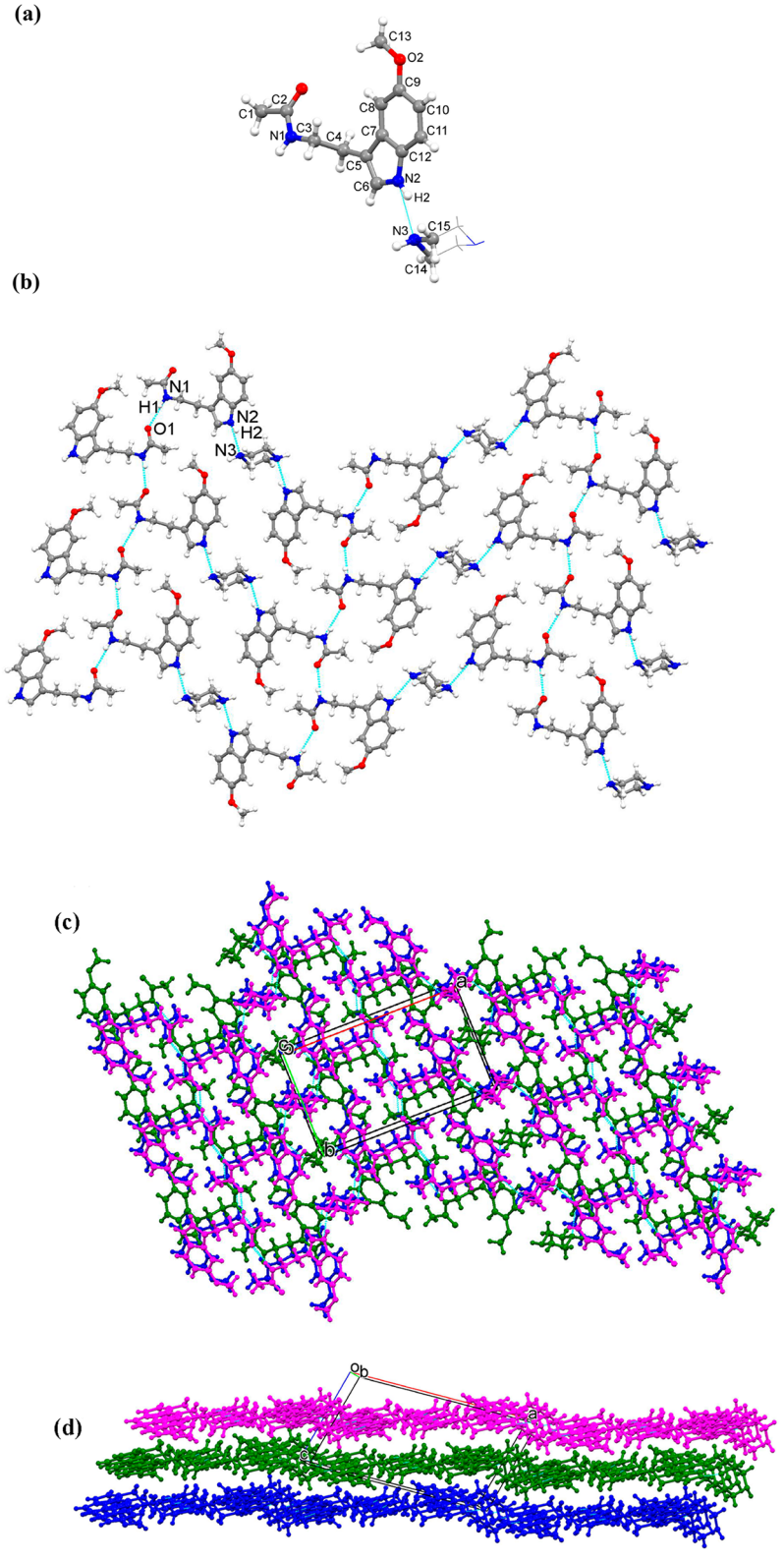

Figure 1. (a) The asymmetric unit, (b) 2D sheet, (c) top, and (d) side view of 3D structure of **MLT−PIP I**.

aliquot was diluted to 1.0 mL with water and was measured with UV−vis spectrophotometry. All the experiments were performed in triplicate (n = 3).

IDR measurements were carried out using the dissolution device ZQY-2 (Shanghai Huanghai Yaojian instrument distribution Co., Ltd.). For each experiment, 500 mL of pH 6.8 phosphate buffer was preheated to 37 °C and stirred at 100 rpm. Approximately 100 mg of MLT or an equivalent amount of cocrystals was compressed to a pellet (5 mm in diameter) using a hydraulic press with a pressure of 0.5 tons for 30 s. The pellets were coated with paraffin wax, leaving one circular face free for dissolution. These pellets were immersed in the dissolution media, and 1.5 mL of samples was withdrawn at a

DOI: 10.1021/acs.cgd.9b01405
Cryst. Growth Des. 2020, 20, 1079−1087

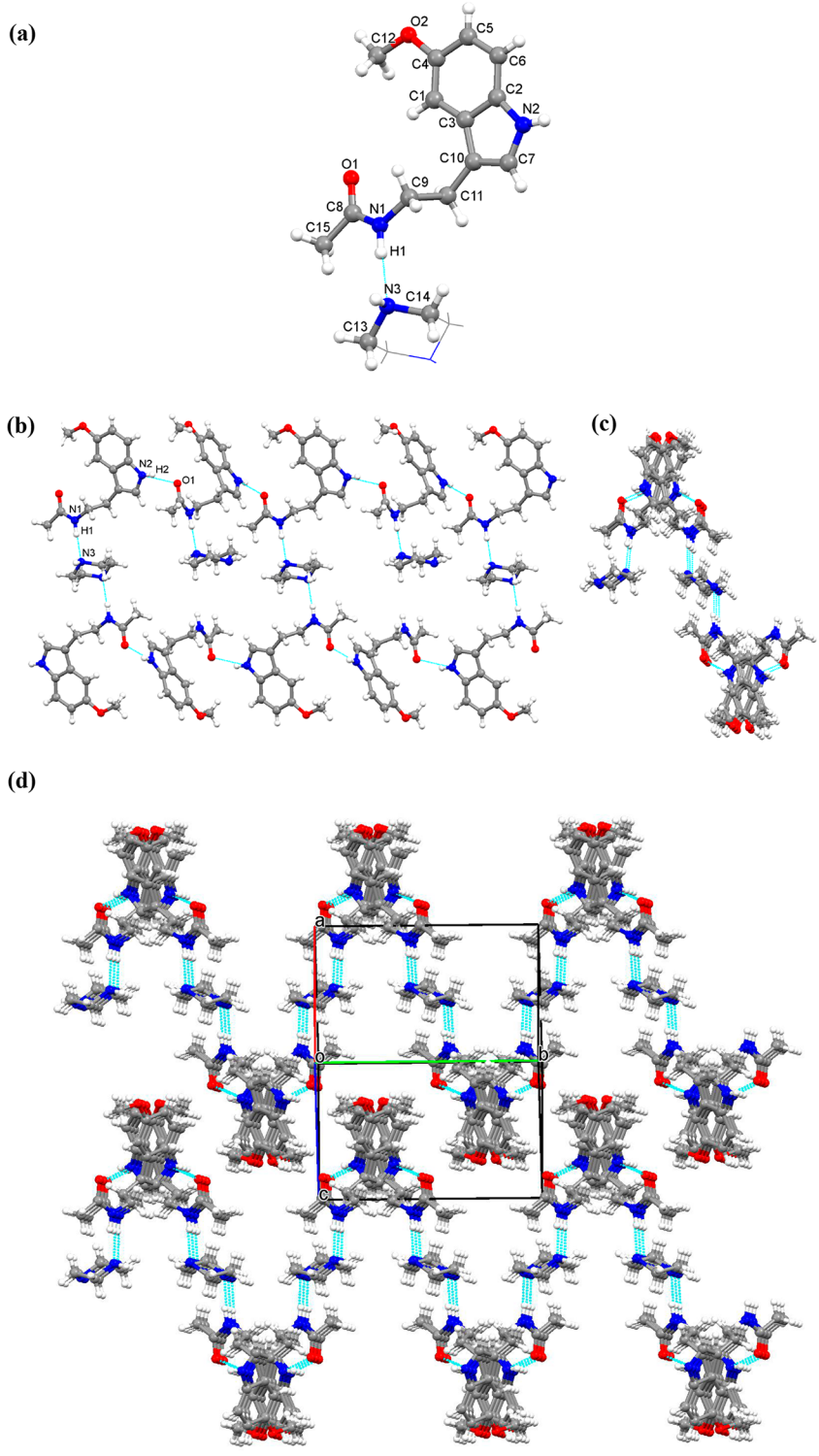

Figure 2. (a) The asymmetric unit, (b) top and (c) side view of 1D chain, and (d) 3D structure of **MLT−PIP II**.

regular time interval. Finally, the intrinsic dissolution rates were calculated from the slope of the initial linear portion of the dissolution curves. All the experiments were carried out in triplicate (n = 3). After the solubility and IDR experiments, the undissolved solids were collected and analyzed by powder X-ray diffraction (PXRD).

Slurry Experiments. Excess powders of both MLT and PIP were added to 1 mL of ethyl acetate, and the resultant suspension was stirred and filtered to obtain a saturated solution. Powder samples of a mixture of **MLT−PIP I** and **MLT−PIP II** with a 1:1 stoichiometric ratio were added to the previously prepared ethyl acetate solution and then slurried under ambient conditions for 20 h. The solid was then filtered and tested by PXRD.

RESULTS AND DISCUSSION

Crystal Structure Analysis. The crystal structures of **MLT−PIP I** and **MLT−PIP II** were determined and resolved to compare their molecular packing and intermolecular interactions.

DOI: 10.1021/acs.cgd.9b01405
Cryst. Growth Des. 2020, 20, 1079−1087

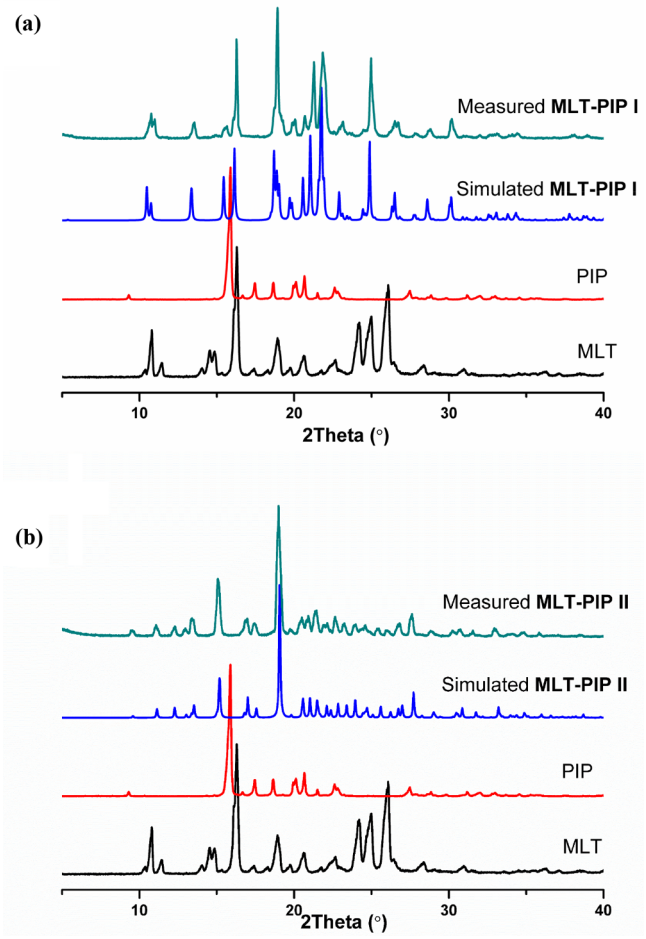

Figure 3. PXRD patterns of (a) **MLT−PIP I** and (b) **MLT−PIP II** systems.

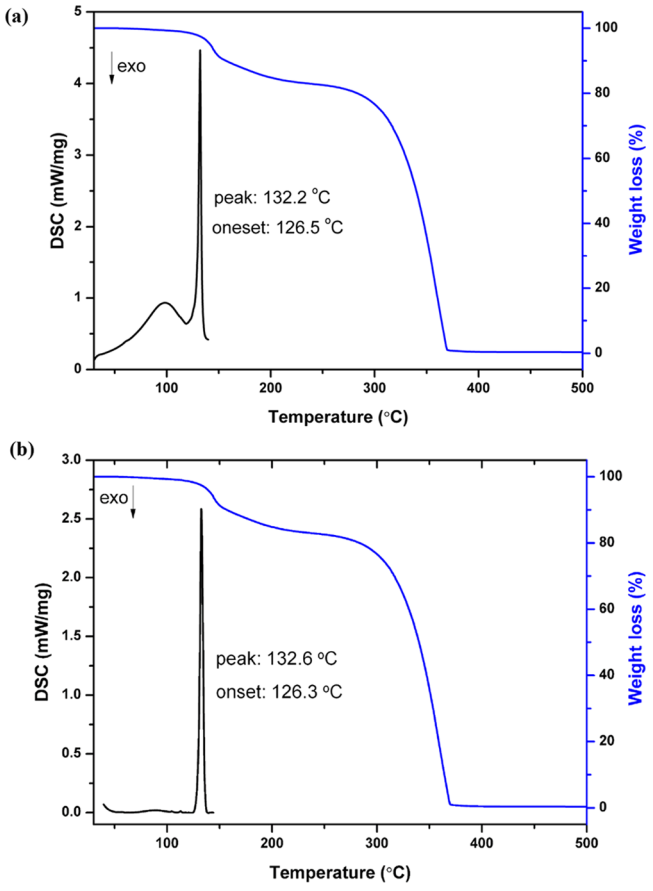

Figure 4. TG/DSC curves of (a) **MLT−PIP I** and (b) **MLT−PIP II**.

Although there are one MLT molecule and half a PIP molecule in the asymmetric units of the crystal structures for both forms, they were solved in different space groups and show different hydrogen bonding modes, molecular packing, and molecular conformations.

MLT−PIP I crystallizes in the space group of monoclinic $P2_1/c$ (Table 1). The MLT molecule connects to the PIP molecule through a N2−H2···N3 hydrogen bond with a N···N distance of 2.976(4) Å (Table 2, Figure 1a). MLT molecules form a molecular chain through N1−H1···O1 hydrogen bonding interaction between amide groups, with the N···O distance of 2.970(2) Å (Table 2). Every other MLT connects to PIP to form a two-dimensional (2D) layer structure (Figure 1b). The neighboring layers are further packed along the *c*-axis to generate the three-dimensional (3D) structure (Figure 1c,d).

In contrast, the crystal structure of **MLT−PIP II** belongs to the monoclinic $P2_1/n$ space group (Table 1). MLT links to PIP through a N1−H1···N3 hydrogen bond with the N···N distance of 2.911(3) Å (Table 2, Figure 2a). MLT molecules form a molecular chain through N2−H2···O1 hydrogen bonding interaction between indole nitrogen and the amide group, with the N···O distance of 2.842(3) Å (Table 2, Figure 2b). The adjacent MLT molecular chains are linked to each other by the hydrogen bonding interactions of every other MLT with PIP to generate a 2D wave-like layer structure (Figure 2c,d). The adjacent layers are further packed together to form the 3D structure (Figure 2d).

The two polymorphs show different crystal packing, in which **MLT−PIP I** shows a layer structure, while **MLT−PIP II** shows a wave-like structure. If we compare the hydrogen bonding distances, we can know the hydrogen bonds in **MLT−PIP II** are shorter and stronger than that in **MLT−PIP I** (Table 2). It suggests that **MLT−PIP II** may be less hydrophilic as its hydrogen bonding sites are more firmly occupied, probably leading to less hygroscopicity and slower dissolution as compared to **MLT−PIP I**.

PXRD and Thermal Analysis. PXRD analysis was performed to check the phase purity of the bulk cocrystal samples. From Figure 3, it can be seen that the PXRD patterns of **MLT−PIP I** and **MLT−PIP II** are totally different from that of either MLT or PIP, indicating the new crystalline phases have been formed. Furthermore, the experimental PXRD pattern of each cocrystal is in good agreement with that calculated from single-crystal diffraction data, which further confirmed their phase homogeneity and bulk purity.

The thermodynamic stability of **MLT−PIP I** and **MLT−PIP II** was investigated by thermogravimetric (TG) analysis, differential scanning calorimetry (DSC), hot-stage microscopy, and variable temperature PXRD analysis. The TG curves of **MLT−PIP I** are similar to that of **MLT−PIP II** (Figure 4). Both of them show a weight loss of 15.7% between 130.5 and 223.4 °C, which is in accordance with losing one-half PIP molecule (calcd 15.6%). The DSC plot of **MLT−PIP II** shows a single endotherm started at 126.3 °C, which is ascribed to the melting of **MLT−PIP II** (Figure 4b). This melting process was also observed between 125 and 130 °C via a hot-stage microscope (Figure 5b). In contrast, a molten liquid film

DOI: 10.1021/acs.cgd.9b01405
Cryst. Growth Des. 2020, 20, 1079−1087

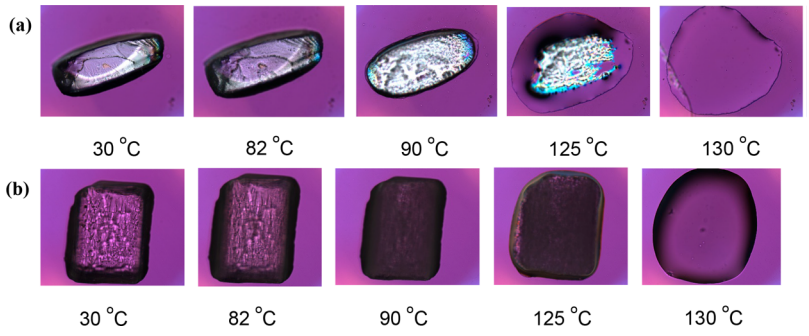

Figure 5. Phase change and melting process of (a) **MLT−PIP I** and (b) **MLT−PIP II** upon heating.

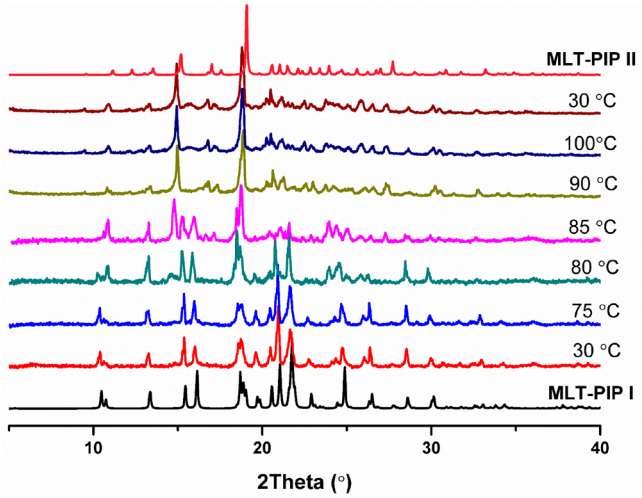

Figure 6. Variable temperature PXRD analysis of a sample of **MLT−PIP I** as a starting form. The decay of **MLT−PIP I** and the formation of **MLT−PIP II** were observed between 80 and 90 °C.

around **MLT−PIP I** was observed at 90 °C by the hot-stage microscope, which is accompanied by a significant change of the appearance of the crystal (Figure 5a). It suggests that **MLT−PIP I** begins to melt at 90 °C, and the melting process of **MLT−PIP I** is accompanied by the recrystallization of **MLT−PIP II** at the same time. Then the resultant **MLT−PIP II** subsequently melts between 125 and 130 °C (Figure 5a). The DSC curve of **MLT−PIP I** shows two endotherm peaks. The first broad peak at 98.3 °C is attributed to the melting process of **MLT−PIP I**, which may cover the exothermic signal of the recrystallization of **MLT−PIP II**. The second peak at 132.2 °C corresponds to the melting of **MLT−PIP II** (Figure 4a). The variable temperature PXRD measurement of **MLT−PIP I** was further conducted to confirm the decay of **MLT−PIP I** and the formation of **MLT−PIP II** during the heating process (Figure 6). The new peaks at 11.1° and 15.1° (2θ) belonging to **MLT−PIP II** began to appear at 80 °C. All the characteristic PXRD peaks of **MLT−PIP I** disappeared, and phase generation of **MLT−PIP II** was complete until 90 °C. As the melting of **MLT−PIP I** and the recrystallization of **MLT−PIP II** occurred at the same time, the halo of a molten was not observed from this series of variable temperature PXRD patterns. Further, when the heated sample was cooled back to 30 °C, **MLT−PIP II** did not convert back to **MLT−PIP I**.

Solubility and Intrinsic Dissolution Rate. Powder dissolution and intrinsic dissolution experiments were conducted to evaluate the solubility and dissolution behavior of the two

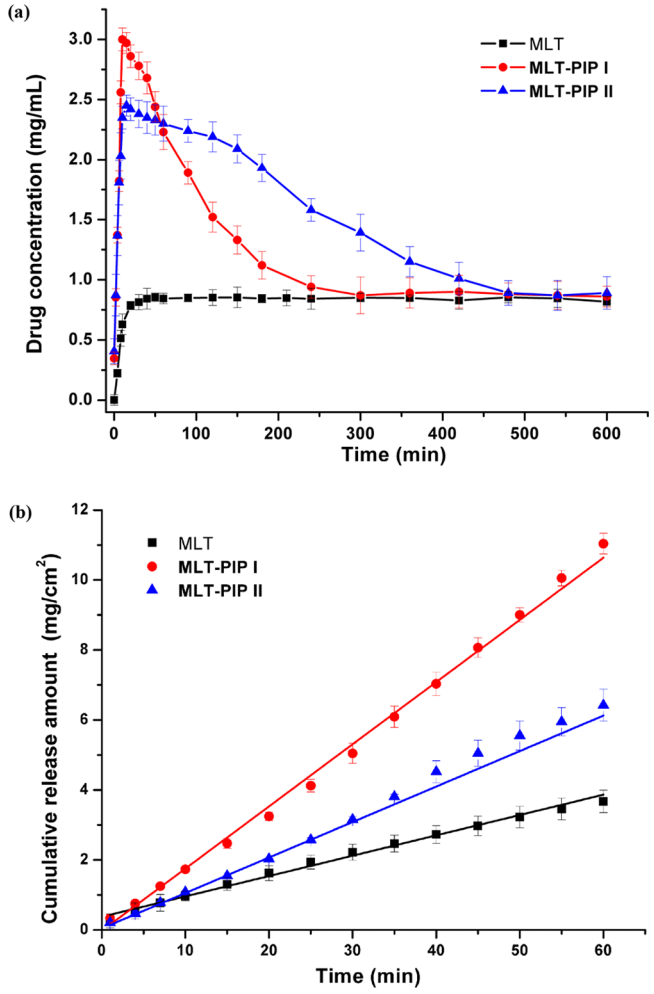

Figure 7. (a) Powder dissolution profiles and (b) IDR profiles for MLT, **MLT−PIP I**, and **MLT−PIP II** at pH 6.8.

cocrystal polymorphs in pH 6.8 buffer which is simulated to the pH microclimate of the human small intestine. Powder dissolution profiles of MLT, **MLT−PIP I**, and **MLT−PIP II** are graphed in Figure 7a in the form of the MLT concentrations (mg/mL) against time (min). As we can see, **MLT−PIP I** and **MLT−PIP II** can achieve a higher MLT concentration with a faster rate. Their dissolution plots reached the maximum apparent solubility (S_{max}) within 30 min, and then gradually decreased with time. This is called a "spring and parachute" effect and is not uncommon for cocrystal systems.[32,33] The maximum apparent solubility (S_{max}) of MLT and the two cocrystal polymorphs obtained from Figure 7a are

DOI: 10.1021/acs.cgd.9b01405
Cryst. Growth Des. 2020, 20, 1079−1087

Table 3. Maximum Solubility (S_{max}) and IDR of MLT and its Cocrystals

	S_{max} (mg·mL^{-1})	IDR (mg·cm^{-2}·min^{-1})
MLT	0.92	0.058
MLT−PIP I	3.24	0.178
MLT−PIP II	2.49	0.101

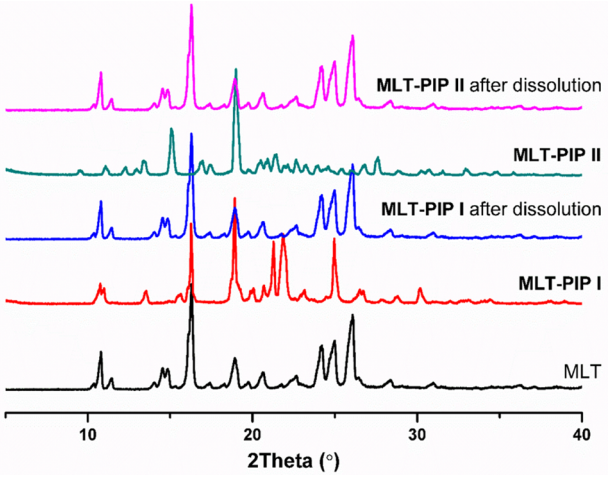

Figure 8. PXRD analysis of **MTN-PPZ I** and **MTN-PPZ II** after powder dissolution experiments.

summarized in Table 3. We can see that the S_{max} values of **MLT−PIP I** and **MLT−PIP II** are 3.5 and 2.8 times as high as that of the parent MLT (Table 3). The supersaturated solutions were formed at the beginning of the dissolution process, and then the concentrations of MLT for **MLT−PIP I** and **MLT−PIP II** are close to that of pure MLT within 5 and 8 h, respectively. It suggests that these two polymorphs convert back to MLT with different rates. The PXRD analysis of the remaining powder after the dissolution experiments confirms the phase conversion of the cocrystals to pure MLT (Figure 8). As a less stable polymorph, **MLT−PIP I** exhibits better apparent solubility, a higher dissolution rate, and faster phase conversion as compared to **MLT−PIP II**.

IDR experiments were performed to quantitatively evaluate the dissolution rate. The IDR curves of MLT, **MLT−PIP I**, and **MLT−PIP II** are given in Figure 7b. Table 3 summarizes the values calculated by least-squares analysis of the linear regions of the IDR curves. The IDR values of 0.178 and 0.101 mg·cm^{-2}·min^{-1} calculated for **MLT−PIP I** and **MLT−PIP II**, are approximately 3.1 and 1.7 times as high as that of the parent MLT (0.058 mg·cm^{-2}·min^{-1}). The order of IDR values can be stated as follows: **MLT−PIP I** > **MLT−PIP II** > MLT, which is consistent with the results of powder dissolution. The PXRD measurements of the recovered solids after IDR tests reveal that both cocrystal polymorphs were not dissociated and maintained their original form.

Dynamic Vapor Sorption (DVS) Study. Both **MLT−PIP I** and **MLT−PIP II** exhibit better solubility and a faster dissolution rate, which is usually relative to a stronger affinity to moisture. DVS experiments were carried out to measure the vapor sorption and desorption behavior. Figure 9 shows the dynamic vapor sorption and desorption isotherms of MLT, **MLT−PIP I**, and **MLT−PIP II**. Under all relative humidity (RH) conditions, **MLT−PIP I** and **MLT−PIP II** absorbed more water than pure MLT. **MLT−PIP I** sorbs more than 0.4% water at 90% RH, demonstrating slight hygroscopicity.

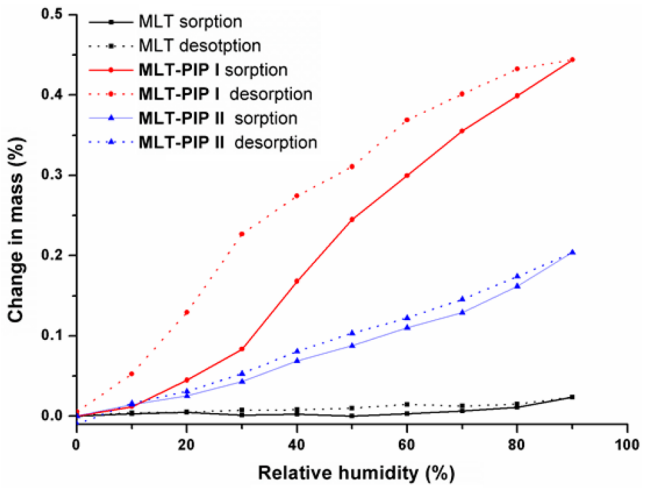

Figure 9. Water sorption/desorption isotherms for MLT, **MLT−PIP I**, and **MLT−PIP II** at 25 °C.

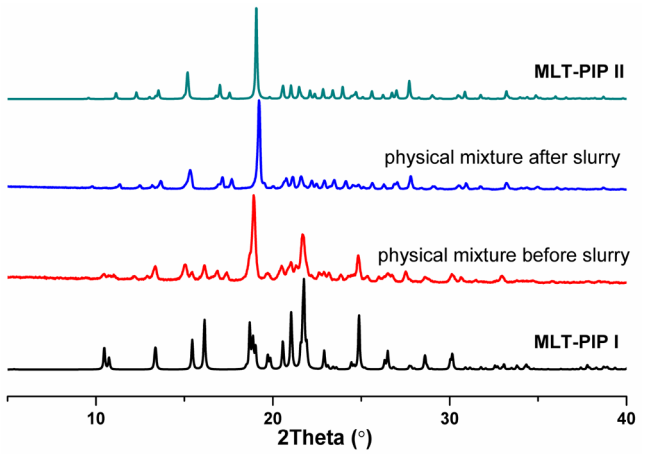

Figure 10. PXRD analysis of **MLT−PIP I**, **MLT−PIP II**, and a physical mixture before and after the slurry conversion experiment.

In contrast, **MLT−PIP II** is considered non-hygroscopic as it only absorbs about 0.2% moisture at high RH. The rank order of the hygroscopicity is **MLT−PIP I** > **MLT−PIP II** > MLT. There is a positive correlation relationship between the hygroscopicity and solubility of the three samples. Furthermore, the sorption−desorption cycles are closed, indicating no phase transformation or dissociation of cocrystals during the DVS measurements. Although the moisture resistance of **MLT−PIP I** and **MLT−PIP II** is not as good as pure MLT, it is still adequate to implement standard processing steps on them.

Relative Stability Analysis. Both experimental and theoretical methods can be used to compare the relative stability of two cocrystal polymorphs. From an experimental perspective, the results of thermal analysis and variable temperature PXRD indicate that **MLT−PIP II** is the stable form under higher temperature. Moreover, **MLT−PIP II** exhibits lower hygroscopicity and solubility as well as slower dissolution as compared to **MLT−PIP I**, demonstrating that it is also more stable at a lower temperature. In addition, a powdered 1:1 mixture of both polymorphs was slurried at room temperature, and the PXRD pattern of the resulting solid only exhibits peaks of **MLT−PIP II**, exhibiting the complete conversion of

DOI: 10.1021/acs.cgd.9b01405
Cryst. Growth Des. 2020, 20, 1079−1087

Table 4. Optimized Unit Cell Parameters, the Total Energies of the Cocrystals, MLT and PIP, and the Lattice Energies of the Cocrystals

	space group	unit cell parameters				E (eV)	E_{latt} (eV)
		a (Å)	b (Å)	c (Å)	β (deg)		
MLT−PIP I	$P2_1/c$	17.4559	9.77772	9.67642	104.417	−1007.0894	−0.4025
MLT−PIP II	$P2_1/n$	8.97975	13.4466	13.5019	101.200	−1007.1576	−0.4706
MLT	$P2_1/c$	8.05305	9.34651	17.3710	97.2700	−827.7005	
PIP	$P2_1/n$	6.22315	5.31304	8.66920	107.371	−178.9865	

MLT−PIP I to **MLT−PIP II** during slurry (Figure 10). It further reveals that **MLT−PIP II** is more stable than **MLT−PIP I** in solution. All these observations suggest that **MLT−PIP I** and **MLT−PIP II** may be monotropically related.

DFT calculations were carried out to optimize the unit cell parameters and evaluate the lattice energies of **MLT−PIP I** and **MLT−PIP II**. Table 4 summarized the optimized unit cell parameters, the total energies of the cocrystals, the relaxed energies of MLT and PIP, as well as the lattice energies of **MLT−PIP I** and **MLT−PIP II**. As we can see, E_{latt} of **MLT−PIP II** (−0.4706 eV) is lower than that of **MLT−PIP I** (−0.4025 eV), suggesting that **MLT−PIP II** is more thermodynamically stable than **MLT−PIP I**. It coincides with the results of the experiments.

CONCLUSIONS

In summary, two polymorphs of a melatonin−piperazine cocrystal (**MLT−PIP I** and **MLT−PIP II**) have been successfully obtained via melt crystallization and liquid-assisted grinding methods. The single crystal structure analysis shows melatonin and piperazine are combined together with 2:1 stoichiometry in both cases. However, the two cocrystal polymorphs exhibit different molecular packing arrangements and hydrogen bonding modes. A combined experimental and theoretical method, including TG, DSC, hot-stage microscopy, variable temperature PXRD, slurry conversion experiments, and DFT calculations, reveals that **MLT−PIP II** is more thermodynamically stable than **MLT−PIP I**. In addition, both cocrystal polymorphs exhibit higher solubility, a faster dissolution rate, and slightly increased hygroscopicity compared to pure MLT, with an order of **MLT−PIP I** > **MLT−PIP II** > MLT. **MLT−PIP II** is considered suitable to be developed into a more efficient formulation of MLT, as it exhibits a significantly improved solubility and dissolution rate with enough stability.

ASSOCIATED CONTENT

Supporting Information

The Supporting Information is available free of charge at https://pubs.acs.org/doi/10.1021/acs.cgd.9b01405.

Materials, general experimental methods and the theoretical calculation details (PDF)

Accession Codes

CCDC 1958004−1958005 contain the supplementary crystallographic data for this paper. These data can be obtained free of charge via www.ccdc.cam.ac.uk/data_request/cif, or by emailing data_request@ccdc.cam.ac.uk, or by contacting The Cambridge Crystallographic Data Centre, 12 Union Road, Cambridge CB2 1EZ, UK; fax: +44 1223 336033.

AUTHOR INFORMATION

Corresponding Author

*E-mail: chenjm37@mail.sysu.edu.cn.

ORCID

Tong-Bu Lu: 0000-0002-6087-4880

Jia-Mei Chen: 0000-0002-3959-901X

Notes

The authors declare no competing financial interest.

ACKNOWLEDGMENTS

This work was financially supported by National Nature Science Foundation of China (No. 21571194) and Key R&D Program of Hebei Province (No. 19227505D).

REFERENCES

(1) Bernstein, J. *Polymorphism in Molecular Crystals*; Clarendon: Oxford, 2002.

(2) Hilfiker, R. *Polymorphism: in the Pharmaceutical Industry*; Wiley-VCH: Weinheim, 2006.

(3) Zhang, W. P.; Chen, D. Y. Crystal structures and physicochemical properties of amisulpride polymorphs. *J. Pharm. Biomed. Anal.* **2017**, *140*, 252−257.

(4) Pandey, K. U.; Dalvi, S. V. Understanding stability relationships among three curcumin polymorphs. *Adv. Powder Technol.* **2019**, *30*, 266−276.

(5) Henwood, S. Q.; Liebenberg, W.; Tiedt, L. R.; Lotter, A. P.; de Villiers, M. M. Characterization of the solubility and dissolution properties of several new rifampicin polymorphs, solvates, and hydrates. *Drug Dev. Ind. Pharm.* **2001**, *27*, 1017−1030.

(6) Viana, A. L. M.; Doriguetto, A. C.; Viana, O. M. M. S.; Ruela, A. L. M.; Freitas, J. T. J.; Souto, B. E. M.; de Araujo, M. B.; de Araujo Paula, F. B. Pharmacokinetics and pharmacodynamics of glimepiride polymorphs. *Int. J. Pharm.* **2018**, *553*, 272−280.

(7) Beyer, T.; Day, G. M.; Price, S. L. The prediction, morphology, and mechanical properties of the polymorphs of paracetamol. *J. Am. Chem. Soc.* **2001**, *123*, 5086−5094.

(8) Byrn, S.; Pfeiffer, R.; Ganey, M.; Hoiberg, C.; Poochikian, G. Pharmaceutical solids: A strategic approach to regulatory considerations. *Pharm. Res.* **1995**, *12*, 945−954.

(9) Lu, J.; Rohani, S. Polymorphism and crystallization of active pharmaceutical ingredients (APIs). *Curr. Med. Chem.* **2009**, *16*, 884−905.

(10) Higashi, K.; Ueda, K.; Moribe, K. Recent progress of structural study of polymorphic pharmaceutical drugs. *Adv. Drug Delivery Rev.* **2017**, *117*, 71−85.

(11) Ke, X.; Ping, Q. N.; Shi, H. Interconversion studies of betamethasone acetate polymorphs. *Drug Dev. Ind. Pharm.* **2005**, *31*, 813−818.

(12) Zhang, G. G. Z.; Gu, C. H.; Zell, M. T.; Burkhardt, R. T.; Munson, E. J.; Grant, D. J. W. Crystallization and transitions of sulfamerazine polymorphs. *J. Pharm. Sci.* **2002**, *91*, 1089−1100.

(13) Thorat, S. H.; Patwadkar, M. V.; Gonnade, R. G.; Vaidhyanathan, R. Capturing a novel metastable polymorph of the anticancer drug gefitinib. *CrystEngComm* **2014**, *16*, 8638−8641.

(14) Aitipamula, S.; Chow, P. S.; Tan, R. B. H. Polymorphism in cocrystals: A review and assessment of its significance. *CrystEngComm* **2014**, *16*, 3451−3465.

(15) Prohens, R.; Barbas, R.; Portell, A.; Font-Bardia, M.; Alcobe, X.; Puigjaner, C. Polymorphism of cocrystals: The promiscuous behavior of agomelatine. *Cryst. Growth Des.* **2016**, *16*, 1063−1070.

DOI: 10.1021/acs.cgd.9b01405
Cryst. Growth Des. 2020, 20, 1079−1087

(16) Schultheiss, N.; Roe, M.; Boerrigter, S. X. M. Cocrystals of nutraceutical p-coumaric acid with caffeine and theophylline: Polymorphism and solid-state stability explored in detail using their crystal graphs. *CrystEngComm* **2011**, *13*, 611−619.
(17) He, H. Y.; Jiang, L. L.; Zhang, Q.; Huang, Y.; Wang, J. R.; Mei, X. F. Polymorphism observed in dapsone-flavone cocrystals that present pronounced differences in solubility and stability. *CrystEngComm* **2015**, *17*, 6566−6574.
(18) Sangtani, E.; Sahu, S. K.; Thorat, S. H.; Gawade, R. L.; Jha, K. K.; Munshi, P.; Gonnade, R. G. Furosemide cocrystals with pyridines: An interesting case of color cocrystal polymorphism. *Cryst. Growth Des.* **2015**, *15*, 5858−5872.
(19) Li, S.; Chen, J. M.; Lu, T. B. Synthon polymorphs of 1:1 co-crystal of 5-fluorouracil and 4-hydroxybenzoic acid: Their relative stability and solvent polarity dependence of grinding outcomes. *CrystEngComm* **2014**, *16*, 6450−6458.
(20) Beyer, C. E.; Steketee, J. D.; Saphier, D. Antioxidant properties of melatonin-an emerging mystery. *Biochem. Pharmacol.* **1998**, *56*, 1265−1272.
(21) Srinivasan, V.; De Berardis, D.; Shillcutt, S. D.; Brzezinski, A. Role of melatonin in mood disorders and the antidepressant effects of agomelatine. *Expert Opin. Invest. Drugs* **2012**, *21*, 1503−1522.
(22) López, G. M.; Guerrero, J.; Ceballo, P. J.; Delgado, M. F. Melatonin in palate tonsils with recurrent acute tonsillitis and tonsillar hypertrophy. *Acta Otorrinolaringol. Espanola* **1997**, *49*, 625−628.
(23) Cajochen, C.; Kräuchi, K.; Wirz-Justice, A. Role of melatonin in the regulation of human circadian rhythms and sleep. *J. Neuroendocrinol.* **2003**, *15*, 432−437.
(24) Castagnino, H. E.; Lago, N.; Centrella, J. M.; Calligaris, S. D.; Farina, S.; Sarchi, M. I.; Cardinali, D. P. Cytoprotection by melatonin and growth hormone in early rat myocardial infarction as revealed by Feulgen DNA staining. *Neuroendocrinol. Lett.* **2002**, *23*, 391−395.
(25) Lissoni, P.; Barni, S.; Mandala, M.; Ardizzoia, A.; Paolorossi, F.; Vaghi, M.; Longarini, R.; Malugani, F.; Tancini, G. Decreased toxicity and increased efficacy of cancer chemotherapy using the pineal hormone melatonin in metastatic solid tumour patients with poor clinical status. *Eur. J. Cancer* **1999**, *35*, 1688−1692.
(26) Dahlitz, M.; Alvarez, B.; Parkes, J.; English, J.; Arendt, J.; Vignau, J. Delayed sleep phase syndrome response to melatonin. *Lancet* **1991**, *337*, 1121−1124.
(27) Chavda, H.; Patel, C.; Anand, I. Biopharmaceutics classification system. *Syst. Rev. Pharm.* **2010**, *1*, 62.
(28) Vlachou, M.; Eikosipentaki, A.; Xenogiorgis, V. Pineal hormone melatonin: Solubilization studies in model aqueous gastrointestinal environments. *Curr. Drug Delivery* **2006**, *3*, 255−265.
(29) Yan, Y.; Chen, J. M.; Lu, T. B. Thermodynamics and preliminary pharmaceutical characterization of melatonin-pimelic acid cocrystal prepared by a melt crystallization method. *CrystEngComm* **2015**, *17*, 612−620.
(30) Shemchuk, O.; Andre, V.; Duarte, M. T.; Braga, D.; Grepioni, F. Mechanochemical preparation of molecular and ionic co-crystals of the hormone melatonin. *CrystEngComm* **2019**, *21*, 2949−2954.
(31) Su, Y.; Xu, J.; Shi, Q.; Yu, L.; Cai, T. Polymorphism of griseofulvin: concomitant crystallization from the melt and a single crystal structure of a metastable polymorph with anomalously large thermal expansion. *Chem. Commun.* **2018**, *54*, 358−361.
(32) Bavishi, D. D.; Borkhataria, C. H. Spring and parachute: How cocrystals enhance solubility. *Prog. Cryst. Growth Charact. Mater.* **2016**, *62*, 1−8.
(33) Surov, A. O.; Solanko, K. A.; Bond, A. D.; Bauer-Brandl, A.; Perlovich, G. L. Cocrystals of the antiandrogenic drug bicalutamide: Screening, crystal structures, formation thermodynamics and lattice energies. *CrystEngComm* **2016**, *18*, 4818−4829.

DOI: 10.1021/acs.cgd.9b01405
Cryst. Growth Des. 2020, 20, 1079−1087